Journal of Materials Chemistry B

Accepted Manuscript

ROYAL SOCIETY OF CHEMISTRY

www.rsc.org/materialsB

Graphic abstract

for

Hydrophilic $Cu_{2-x}Se$/reduced graphene oxide nanocomposites with tunable plasmonic properties and their applications in cellular dark-field microscopic imaging

Wen Long Li, [a] Shao Qing Lie, [a] Yu Qing Du, [b] Xiao Yan Wan, [b] Ting Ting Wang, [b] Jian Wang, [b] Cheng Zhi Huang * [a b]

a Key Laboratory of Luminescent and Real-Time Analytical Chemistry (Southwest University), Ministry of Education, College of Chemistry and Chemical Engineering, Southwest University, Chongqing 400715, China
b College of Pharmaceutical Science, Southwest University, Chongqing 400715, China
* Corresponding Author. E-mail: chengzhi@swu.edu.cn

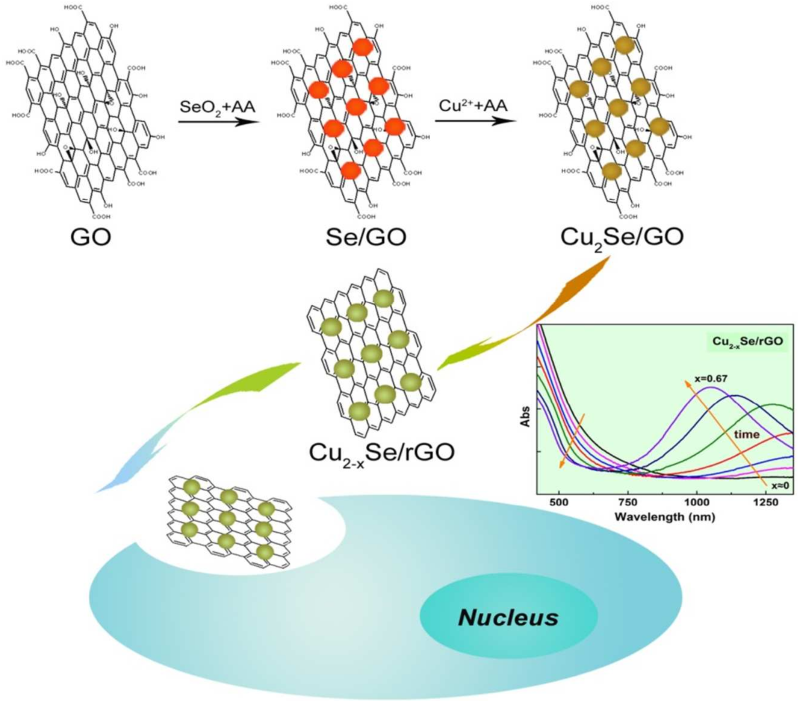

We report a facile and green aqueous chemical approach to one-pot fabricate $Cu_{2-x}Se$/rGO nanocomposites at room temperature, with tunable plasmonic properties as well as favorable biocompatibility, and further exploit them as efficient dark-field light scattering probes for cancer cell imaging *in vitro*.

Journal Name

RSCPublishing

ARTICLE

Cite this: DOI: 10.1039/x0xx00000x

Received 00th January 2012,
Accepted 00th January 2012

DOI: 10.1039/x0xx00000x

www.rsc.org/

Hydrophilic $Cu_{2-x}Se$/reduced graphene oxide nanocomposites with tunable plasmonic properties and their applications in cellular dark-field microscopic imaging

Wen Long Li, [a] Shao Qing Lie, [a] Yu Qing Du, [b] Xiao Yan Wan, [b] Ting Ting Wang, [b] Jian Wang [b] and Cheng Zhi Huang* [a b]

A facile aqueous chemical approach is developed for one-pot synthesis of the nanocomposites of heavily doped semiconductor nanoparticles ($Cu_{2-x}Se$ NPs) and reduced graphene oxide (rGO) at room temperature, wherein the reduction of GO and the *in situ* growth of $Cu_{2-x}Se$ NPs on rGO sheets occur simultaneously. The as-prepared $Cu_{2-x}Se$/rGO nanocomposites exhibit a well-defined near-infrared (NIR) localized surface plasmon resonance (LSPR), which arises from free carriers (holes) and could be tuned from 1360 to 1050 nm by varying the reaction time, owing to the increase of the free carriers density in the valence band of $Cu_{2-x}Se$ NPs. This approach not only offers an efficient strategy to synthesize the self-doped $Cu_{2-x}Se$/rGO nanocomposites with strong and tunable NIR absorption, but also develops new light scattering nanoprobes with good biocompatibility as well as unique optical properties for *in vitro* cellular dark-field microscopic imaging (iDFM).

Introduction

Copper chalcogenides (i.e., $Cu_{2-x}S$, $Cu_{2-x}Se$ and $Cu_{2-x}Te$) have attracted much interest and have been applied in a wide range of fields, including electronics,[1, 2] optoelectronic devices,[3-5] batteries,[6] catalysis[7, 8] and chemical sensing,[9, 10] due to their special eletrical and optical properties. Interestingly, copper chalcogenides exhibit a well-defined localized surface plasmon resonance (LSPR) in the near-infrared (NIR) region,[11-20] which is generally associated with metal nanostructures, and has recently been applied in photoacoustic imaging[21, 22] and photothermal therapy.[17, 23-25] Opposite to the LSPR in metals,[26] which is attributed to the collective oscillation of free electrons, the NIR LSPR in these heavily doped copper chalcogenides arises from free carriers (holes) provided by cation vacancies, which are generated *via* oxidation in nonstoichiometric copper chalcogenides. Intriguingly, the plasmonic absorption of copper chalcogenides can be dynamically tuned by altering the free carriers density, carried out by varying their size, geometry, phase and morphology, [15-17, 27] and could be further explored in rich energy- and plasmonic-related applications. Meanwhile, some efforts have been invested in the study of copper chalcogenides-based hybrid nanoparticles (NPs), an interesting class of colloidal nanostructures, which combine different material properties in one nanosystem and exhibit more excellent performance than the individual one. Hu *et al.* designed sub-10 nm Fe_3O_4@$Cu_{2-x}S$ core-shell NPs as ideal multifunctional probes for MRI imaging, infrared thermal imaging, and photothermal therapy.[28] Swihart *et al.* synthesized Au-$Cu_{2-x}Se$ heterodimer NPs and utilized the LSPR in Au-$Cu_{2-x}Se$ NPs for both deep tissue photoacoustic imaging *in vivo* and dark field optical imaging *in vitro*.[29]

It's worth noting that copper sulfide/reduced graphene oxide hybrids have captured considerable attention owing to their potential applications in optoelectronic devices,[30, 31] sensors[32, 33] and catalysts.[34] Graphene, a sp^2-hybrid carbon atom sheet, has been an attractive scaffold for anchoring nanoparticles to form hybrid materials with improved properties,[35-39] due to its large surface area, good biocompatibility, superior electrical conductivity and ultrafast heterogeneous electron-transfer rate. However, these reports concerning copper sulfide/reduced graphene oxide nanocomposites don't involve in the studies on the NIR LSPR absorption, although copper sulfide with strong NIR LSPR has been successfully developed in photoacoustic imaging[21] and photothermal therapy.[24, 25]

It is easy to understand that the working route to prepare copper chalcogenides will exert strong effects on their further assembly into the hybrids of copper chalcogenide/reduced graphene oxide. Up to now, copper selenides have been usually synthesized through an oil-phase, high-temperature and complicated procedure, even under the protection of N_2 or Ar atmosphere.[1, 3] These hydrophobic products may greatly restrict their potential applications *in vitro* or *in vivo*. Although hydrophobic NPs could be intelligently dispersed in aqueous media by encapsulating with amphiphilic polymers to form very stable micelles in water,[22, 23] they are in reality constrained by the undesirable surface modification and consequent size increase of NPs. Therefore, new available water-phase methods for synthesizing hydrophilic copper selenides or their hybrids with excellent performance are urgently expected.

Herein, we report a facile aqueous chemical approach at room temperature for one-pot synthesis of $Cu_{2-x}Se$/reduced graphene oxide ($Cu_{2-x}Se$/rGO) nanocomposites with an intense well-defined NIR LSPR, during which the reduction of GO and the *in situ* growth of $Cu_{2-x}Se$ NPs on rGO sheets occur simultaneously. With the introduction of ascorbic acid (AA), a green natural product, which serves not only as a mild reducing agent, but also as a capping reagent, individual $Cu_{2-x}Se$ NPs are uniformly decorated on the rGO sheets without apparent aggregation. A possible growth mechanism for $Cu_{2-x}Se$/rGO nanocomposites is proposed by analyzing the time evolution of their optical absorption spectra. Owing to the nonstoichimetric composition of cubic $Cu_{2-x}Se$ NPs decorated on rGO, $Cu_{2-x}Se$/rGO nanocomposites present the LSPR band in the NIR region, which could be well-tuned from 1360 to 1050 nm by adjusting the density of free carriers (holes) through the reaction time, with the preservation of the crystal phase and morphology of $Cu_{2-x}Se$ NPs. Furthermore, the as-prepared $Cu_{2-x}Se$/rGO nanocomposites exhibit good biocompatibility as well as unique dark-field light scattering properties, and are well applied as efficient probes for cellular dark-field microscopic imaging (iDFM) *in vitro*.

Results and discussion

Preparation and characterization of $Cu_{2-x}Se$/rGO nanocomposites.

Cubic $Cu_{2-x}Se$/rGO nanocomposites with high purity were firstly prepared by a green and facile aqueous chemical route at room temperature, which can precisely control the reaction microenvironment and the growth orientation of $Cu_{2-x}Se$ NPs. In $Cu_{2-x}Se$/rGO nanocomposites, the rGO sheets act as flexible two-dimensional supports for anchoring $Cu_{2-x}Se$ NPs. SEM and TEM images of the nanocomposites show that individual spherical $Cu_{2-x}Se$ NPs are uniformly and randomly decorated on the surface of rGO sheets or are enwrapped in rGO sheets without apparent aggregation (Fig. 1). Moreover, neither unassembled NPs nor free rGO sheets could be observed, indicating a high assembly efficiency of $Cu_{2-x}Se$ NPs. High-resolution TEM (HRTEM) image (Fig. 1D) shows that the lattice fringes have an interlayer distance of 0.22 nm, corresponding to the (220) plane of cubic $Cu_{2-x}Se$.[3, 4] Furthermore, the HRTEM result indicates these NPs are single crystals. The diffraction pattern in selected area electron diffraction (SAED) of $Cu_{2-x}Se$/rGO nanocomposites (inset of Fig. 1D) exhibits sharp diffraction rings assigning to the specific crystalline planes of $Cu_{2-x}Se$ NPs and rGO.

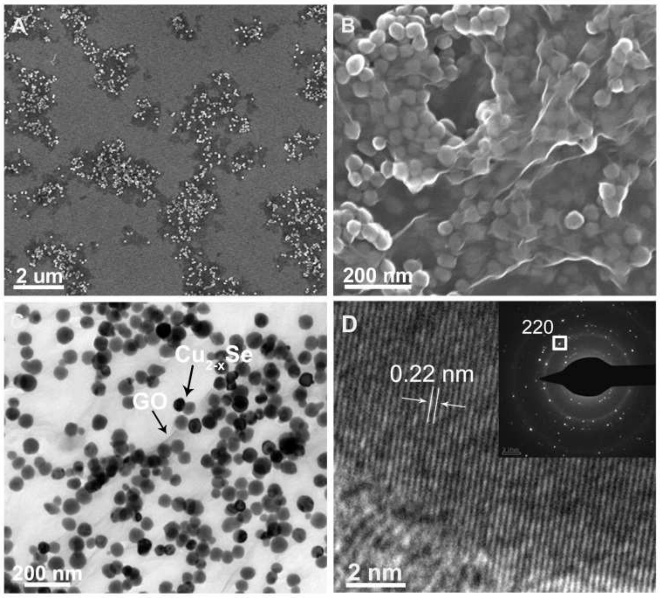

Fig. 1. Characterization of the as-prepared $Cu_{2-x}Se$/rGO nanocomposites. (A) SEM, (B) magnified SEM, (C) TEM and (D) HRTEM images of $Cu_{2-x}Se$/rGO nanocomposites. The inset in (D) shows the SAED pattern of $Cu_{2-x}Se$/rGO nanocomposites.

The average size of $Cu_{2-x}Se$ NPs is about 53 nm with size distribution of 33-73 nm (Fig. S1), that is consistent with that of pure $Cu_{2-x}Se$ NPs (Fig. S2). The atomic force microscopy (AFM) images (Fig. S3) also provide the diameter of $Cu_{2-x}Se$ NPs and the thickness of rGO. The energy dispersive X-ray spectroscopy (EDX) analysis (Fig. S4) confirms the presence of Cu, Se, C and O elements, and the Cu/Se atomic ratio is about 1.33 (x=0.67), suggesting a high copper vacancy in $Cu_{2-x}Se$ NPs.[8] The oxygen content in the as-prepared $Cu_{2-x}Se$/rGO nanocomposites is quite low due to the reduction of GO. Notably, different assembly densities of $Cu_{2-x}Se$ NPs on rGO sheets can be controllably obtained by changing the amount of GO (Fig. S5).

Fig. 2A shows the XRD patterns of the GO and $Cu_{2-x}Se$/rGO nanocomposites. It is found that pristine GO (Fig. 2A, black curve) exhibits a strong crystalline peak at 11.3°, corresponding to the (002) interplanar spacing of GO. For $Cu_{2-x}Se$/rGO nanocomposites (Fig. 2A, red curve), the characteristic peak of GO disappeared, suggesting the reduction of GO.[32] The new diffraction peaks at 27.0°, 31.0°, 45.0°, 53.3°, 65.6°, 72.1°, 83.0° are consistent with the (111), (200), (220), (311), (400), (331) and (422) planes of cubic phase $Cu_{2-x}Se$, respectively.[3, 4] No desirable characteristic peaks are observed for impurities, indicating the formation of cubic $Cu_{2-x}Se$ with high crystallinity. Furthermore, the absence of the diffraction peak of rGO (d-spacing 3.7 Å at $2\theta = 24.0°$) suggests the regular stacks of GO are exfoliated,[40] and $Cu_{2-x}Se$ NPs anchored on rGO sheets prevents the further agglomeration of rGO sheets.[34, 41]

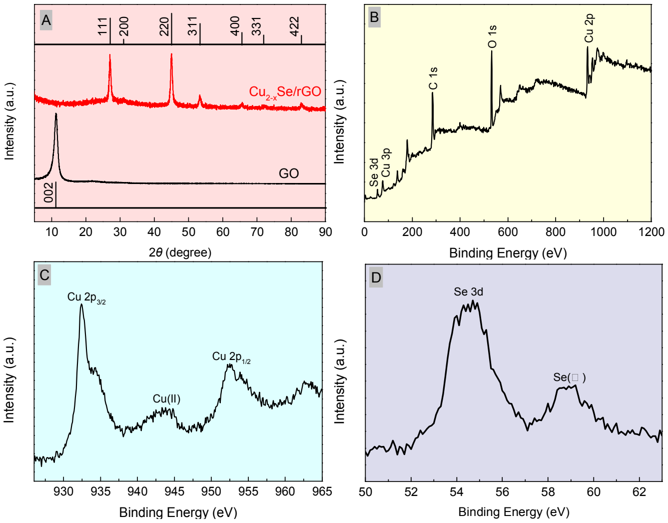

Fig. 2. Crystal structure and value state of $Cu_{2-x}Se$ decorated on rGO sheets. (A) XRD patterns of GO and $Cu_{2-x}Se$/rGO nanocomposites. Typical XPS spectra of $Cu_{2-x}Se$/rGO nanocomposites: (B) survey spectrum, (C) Cu 2p region XPS spectrum, (D) Se 3d region XPS spectrum.

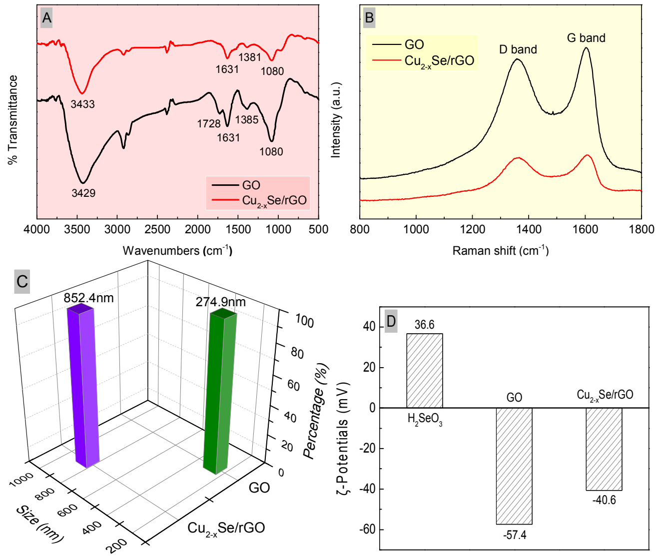

Fig. 3. Confirmation of the reduction of GO and the formation of $Cu_{2-x}Se$/rGO nanocomposites. (A) FTIR spectra and (B) Raman spectra of GO and $Cu_{2-x}Se$/rGO nanocomposites. (C) Dynamic light scattering (DLS) and (D) ζ-potential measurements of GO and $Cu_{2-x}Se$/rGO nanocomposites.

Crucial information on the chemical composition and valence state could be acquired from XPS analysis. The typical survey of XPS spectra (Fig. 2B) clearly shows the peaks of Cu 2p, Se 3d, C 1s and O 1s. The C 1s and O 1s peaks mainly come from rGO.[34] Fig. 2C shows the binding energies of Cu $2p_{3/2}$ and Cu $2p_{1/2}$ at 932.4 and 952.5 eV, in agreement with typical values for Cu^+ in $Cu_{2-x}Se$.[1, 3, 4] The Cu 2p peak has a satellite line at 940 - 945 eV due to Cu (II).[1, 4] The binding energy for Se 3d is 54.7 eV (Fig. 2D), which is representative of lattice Se^{2-}.[1, 3, 4] The small peak at 58.9 eV points to an oxidation state of Se (possibly SeO_2).[1, 4] The C1s spectrum of $Cu_{2-x}Se$/rGO nanocomposites could be divided into three peaks at 284.8, 286.9, and 288.5 eV (Fig. S6), which are associated with C-C, C-O (epoxy and alkoxy) and C=O (carbonyl), respectively.[34] Compared with C1s spectra of GO reported in the literature,[42, 43] the dramatic decreases of peak intensities of oxygen functional groups in the C 1s XPS spectrum confirms that GO has been converted to graphene.

Fig. 3A shows the FTIR spectra of GO and $Cu_{2-x}Se$/rGO nanocomposites. The oxygen-containing functional groups of GO afford bands at 3430, 1728, 1385 and 1080 cm^{-1}, which are associated with the -OH vibration, the C=O stretching vibration, the C-O-H deformation and the alkoxy C–O stretching vibration peaks, respectively.[42] The peak at 1631 cm^{-1} (aromatic C=C) can be assigned to the skeletal vibrations of unoxidized graphite domains.[43, 44] In the spectrum of $Cu_{2-x}Se$/rGO nanocomposites, the difference from that of GO is evidenced by the entire disappearance of the C=O stretching vibration peak and the dramatic decreases of other oxygen-containing functional groups peaks, which confirm that most oxygen functionalities have been removed and GO has been effectively reduced (also seen in the TGA and DTG curves of $Cu_{2-x}Se$/rGO nanocomposites, Fig. S7).[42]

Raman spectroscopy was further performed to characterize GO and $Cu_{2-x}Se$/rGO nanocomposites. Fig. 3B shows both GO and $Cu_{2-x}Se$/rGO nanocomposites exhibit two characteristic main peaks: the D band at 1358 cm^{-1}, arising from a breathing mode of κ-point photons of A_{1g} symmetry; the G band at 1589 cm^{-1}, arising from the first order scattering of the E_{2g} phonon of sp^2 C atoms.[32] Compared with GO, the value of I_D/I_G slightly increases for $Cu_{2-x}Se$/rGO nanocomposites, revealing a change in the electronic conjugation state during the reduction process of GO.[42]

For better elucidating the *in situ* synthesis of $Cu_{2-x}Se$/rGO nanocomposites, dynamic light scattering (DLS) and ζ-potential measurements were performed. As shown in Fig. 3C, GO has the main size distribution of 274.9 nm, while $Cu_{2-x}Se$/rGO nanocomposites have the main size distribution of 852.4 nm, respectively. Both GO and $Cu_{2-x}Se$/rGO nanocomposites exhibit a pure size distribution and almost no unconsidered size distribution emerges (Fig. S8). The obvious changes of size distributions confirm the successful synthesis of $Cu_{2-x}Se$/rGO nanocomposites.

Fig. 3D shows that pure GO possesses a ζ-potential of -57.4 mV, and the value slightly increases to -40.6 mV for $Cu_{2-x}Se$/rGO nanocomposites (Fig. S9), respectively. Interestingly, H_2SeO_3 possesses a ζ-potential of 36.6 mV (Fig. 3D), relatively high positive charge, so H_2SeO_3 could combine to GO sheets through molecular electrostatic attraction. H_2SeO_3 was reduced to Se NPs by AA, thus Se NPs were formed on GO sheets *in situ* (Se/GO nanocomposites).[45] When both $CuSO_4$ and AA added, Cu^{2+} could be reduced to Cu^+ *via* AA, resulting in the diffusion of Cu^+ into the surface of Se NPs and catalyzing the disproportion of Se^0 to Se^{4+} and Se^{2-}.[46] Cu^+ reacted with Se^{2-} to produced Cu_2Se NPs on GO sheets *in situ* (Cu_2Se/GO nanocomposites). On exposure to air, stoichiometric Cu_2Se was oxidized to more thermodynamically stable nonstoichiometric $Cu_{2-x}Se$, with an intense NIR absorption.[1, 14] Meanwhile, the reduction of GO was performed in the aqueous solution,

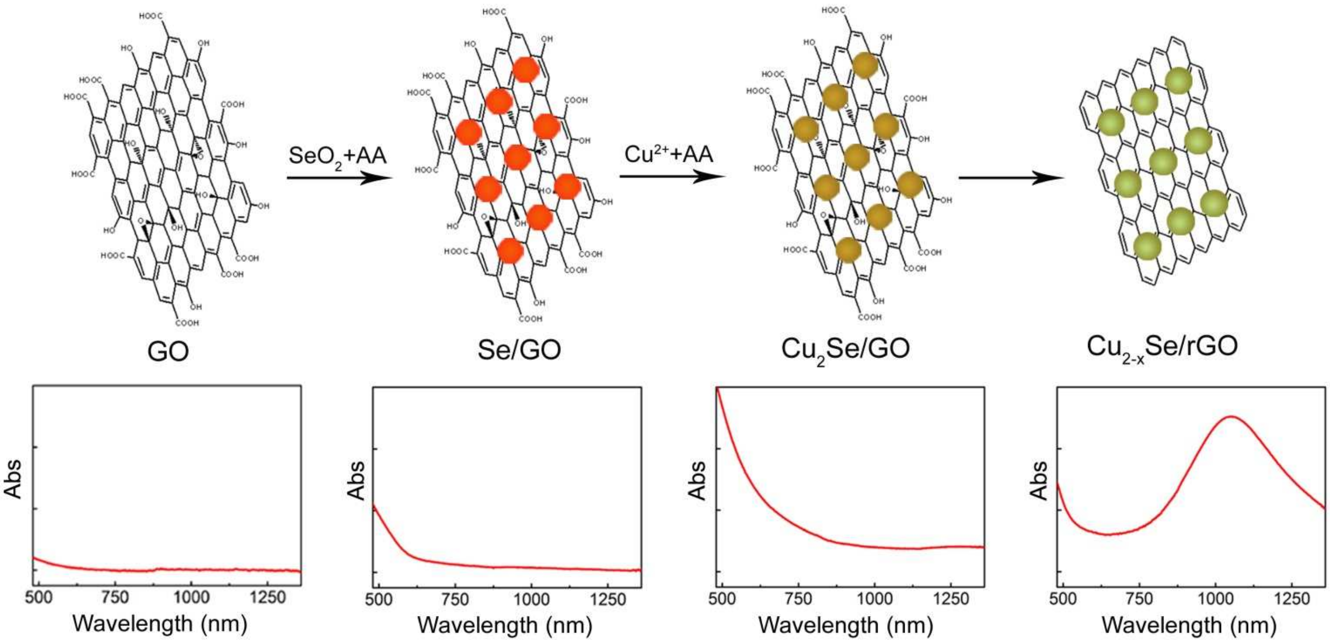

Scheme 1. Simplified experimental procedure for the synthesis of Cu$_{2-x}$Se/rGO nanocomposites. During the growth, the products present the time evolution of the NIR absorption spectra (bottom), which is a LSPR in Cu$_{2-x}$Se/rGO nanocomposites finally.

thereby generating Cu$_{2-x}$Se/rGO nanocomposites (Fig. S10). The growth process can be further understood by investigating the time-dependent NIR absorption evolution of the intermediate products at different intervals of time (Scheme 1).

NIR LSPR in Cu$_{2-x}$Se/rGO nanocomposites.

GO has two UV-vis absorption bands centered at 227 and 300 nm, and no distinct absorption in the NIR region (Fig. S11). After the formation of Cu$_{2-x}$Se/rGO nanocomposites, however, the two UV-vis absorption bands of GO have been disappeared and a new absorption peak shows up around 238 nm, which comes from rGO.[42] Another visible band appears at 470 nm in Cu$_{2-x}$Se/rGO nanocomposites, and a NIR absorption exhibits an intense peak at 1050 nm, compared with GO.

By comparing the absorption of both Cu$_{2-x}$Se/rGO nanocomposites and pure Cu$_{2-x}$Se NPs (Fig. 4A), it is obvious that the absorption above 400 nm, especially in the NIR region, is attributed to Cu$_{2-x}$Se NPs since rGO exhibits negligible absorption in this region (Fig. S12), while the visible absorption between 400 and 600 nm should be assigned to the direct band gap transition of Cu$_{2-x}$Se NPs and the NIR absorption to a surface plasmon resonance.[13, 23] The as-prepared Cu$_{2-x}$Se/rGO nanocomposites have a high copper vacancy in Cu$_{2-x}$Se NPs and the high concentration of free carrier (holes) leads to a strong LSPR in the NIR region.[14]

To further expound the LSPR behavior of Cu$_{2-x}$Se/rGO nanocomposites in the NIR region, we studied the effect of the solvent medium on the absorption band position. The first refractive index sensing experiment was performed with dispersing the nanocomposites in three organic solvents (polar

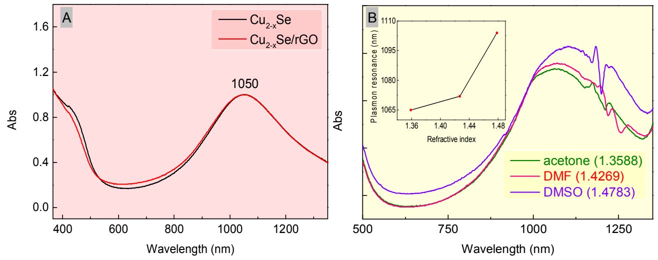

Fig. 4. LSPR feature of Cu$_{2-x}$Se/rGO nanocomposites. (A) LSPR of pure Cu$_{2-x}$Se NPs and Cu$_{2-x}$Se/rGO nanocomposites (The intensity of the absorbance peak centered at 1050 nm was normalized). (B) Cu$_{2-x}$Se/rGO nanocomposites dispersed in three different solvents: acetone, DMF, DMSO, with refractive indices of 1.3588, 1.4269, and 1.4783, respectively. The inset shows the red-shift in the LSPR maximum with increasing refractive index of the solvent. From the inset, the LSPR sensitivity is estimated to be ~326 nm/RIU, which is slightly higher than values for the silver NPs arrays that are commonly used for LSPR sensing.[47]

aprotic solvents): acetone, DMF, DMSO, with refractive indices of 1.3588, 1.4269, and 1.4783, respectively. The NIR absorption band red-shifts with increasing solvent refractive index (Fig. 4B), as expected from an LSPR feature.[5, 12, 14] This magnitude of spectral shift can also be found in alcohols (polar protic solvents, Fig. S13).

Tunable properties of the NIR LSPR in $Cu_{2-x}Se$/rGO nanocomposites.

With increasing reaction time, the vis-NIR absorption spectra (above 400 nm) of $Cu_{2-x}Se$/rGO nanocomposites change gradually. For 2 min, the nanocomposites are characterized with low intensity visible absorption and negligible NIR LSPR absorption, around 1360 nm (black curve in Fig. 5A), a typical feature of Cu_2Se, i.e., x ≈ 0.[14] As the reaction proceeds, air exposure leads to the development of a NIR band in $Cu_{2-x}Se$/rGO nanocomposites that gradually gains intensity and blue-shifts, down to 1050 nm (Fig. 5A). Upon reaction we also observed that the intensity of the direct band gap transition below 600 nm for $Cu_{2-x}Se$/rGO nanocomposites decreases, likely affecting excitonic transitions in $Cu_{2-x}Se$ NPs.[14]

The XRD patterns displayed in Fig. 5B indicate that the crystal structures of $Cu_{2-x}Se$/rGO nanocomposites with different reaction time were both cubic. All peaks could be assigned, suggesting that no crystalline impurities are present during the air exposure.[13] The main peaks at 27.0°, 45.0°, and 53.3° slightly shift to higher 2θ angles indicating a decrease in the lattice parameters as the reaction proceeds.[1, 14] In both cases, SEM images confirm that $Cu_{2-x}Se$ NPs preserve their original shape and size during reaction (Fig. S14).

The LSPR frequency depends on the free carrier density in $Cu_{2-x}Se$/rGO nanocomposites. On exposure to air, cationic Cu expelled from the crystal lattice to the surface of the NPs (presumably formed a thin CuO layer or remained bound to the surface), creating cation vacancies in the lattice without altering the actual structure.[13, 14] The cation vacancies are responsible for the formation of free carriers (holes) in the nonstoichiometric NPs, while the lattice remains practically unperturbed, as the crystal symmetry does not change. [13] This is why the crystal structures of $Cu_{2-x}Se$/rGO nanocomposites were both cubic during the reaction process. An increasing density of cation vacancies (free carriers in the valence band of NPs) is generated with the time of air exposure increasing.[12, 14] This leads to a high free carrier absorption in the NIR region. A high concentration of free carriers in the NPs, localized in a confined space, undergoes collective oscillations when excited with an electromagnetic field of appropriate frequency, giving rise to a LSPR band in $Cu_{2-x}Se$ NPs. The NIR band progressively gains intensity and blue-shifts with increasing free carrier density, expected for an LSPR behavior.[12, 14]

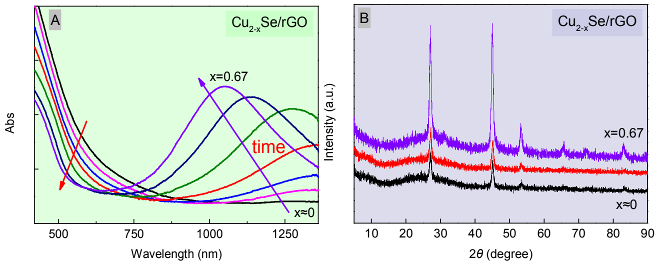

Fig. 5. Optical absorption and crystal structure of $Cu_{2-x}Se$/rGO nanocomposites during reaction. (A) Time evolution of the vis-NIR absorption spectra of $Cu_{2-x}Se$/rGO nanocomposites synthesized for 2 min, 5 min, 10 min, 1 h, 4 h, 7 h, and 10 h, respectively. With increasing reaction time, x gradually increases, from x ≈ 0 (black curve) to x = 0.67 (violet curve). (B) XRD patterns of $Cu_{2-x}Se$/rGO nanocomposites shown in (A) during the reaction process. From the black to the violet curve, the patterns are recorded for 2 min (x ≈ 0, black curve), 1h (x = 0.39, red curve), 10h (x = 0.67, violet curve) of reaction process.

In vitro iDFM of $Cu_{2-x}Se$/rGO nanocomposites on cancer cells.

Resonance light scattering features from noble metal NPs are specific and many fascinating applications of light scattering have been reported in nanoalloys growth and cell imaging,[48-52] and it is interesting that carbon nanomaterials can enhance the light scattering imaging efficiency.[50] In such case, herein we further make efforts to investigate the light scattering properties of $Cu_{2-x}Se$/rGO nanocomposites for the first time, and apply them as optical probes for cellular imaging under dark field microscopy.

$Cu_{2-x}Se$/rGO nanocomposites show an intense light scattering peak located at 470 nm in the blue region, and the light scattering intensity is much strong compared with $Cu_{2-x}Se$ NPs (Fig. S15). From dark-field light scattering images, we can see that pure GO cannot supply any effective optical signals and hard to be observed under a dark-field scattering microscopy, while individual $Cu_{2-x}Se$ NPs scatter weak blue light (Fig. S16). For $Cu_{2-x}Se$/rGO nanocomposites, the assembled $Cu_{2-x}Se$ NPs likely dress an optically visible ‘‘coat’’ on the rGO sheets and provide optical signals for illuminating rGO in optical imaging systems, demonstrating the prepared nanocomposites could be potentially used as biocompatible agents for *in vivo* imaging and cargo transporting.[50] It is worthwhile mentioning that such nanocomposites exhibit exciting mutual properties that are

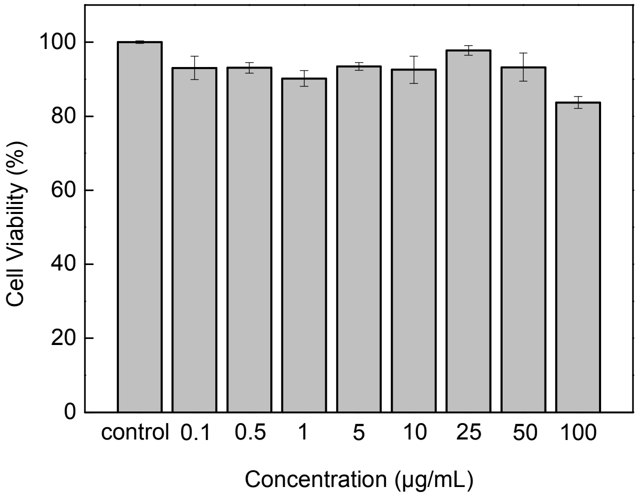

Fig. 6. Cell viabilities estimated by the CCK-8 test *versus* incubation different concentration (0-100 μg/mL) of $Cu_{2-x}Se$/rGO nanocomposites in HEp-2 cells at 37 ℃ for 24 h.

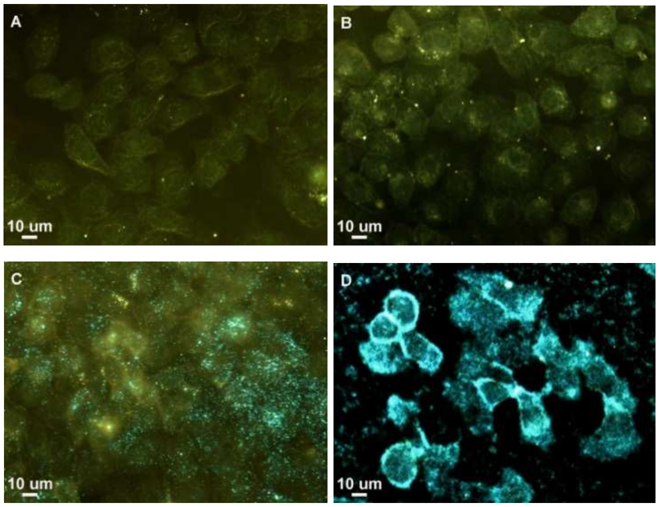

Fig. 7. *In vitro* dark-field light scattering images of HEp-2 cells (A) and after interacting with GO (B), $Cu_{2-x}Se$ NPs (C), and $Cu_{2-x}Se$/rGO nanocomposites (D). (Scale bar = 10μm; 40× objective lens).

significantly different from those of the individual ones, such as the brighter scattering light from the assembled $Cu_{2-x}Se$ NPs on rGO sheets, and the visible profile of rGO through $Cu_{2-x}Se$ NPs' decoration.[50, 51]

The favorable biocompatibility of graphene makes $Cu_{2-x}Se$/rGO nanocomposites possibly suitable for bioapplication to cells. Low cytotoxicity is detected for $Cu_{2-x}Se$/rGO nanocomposites even for concentration as high as 100 μg/mL (Fig. 6), demonstrating good biocompatibility of the as-prepared nanocomposites. $Cu_{2-x}Se$/rGO nanocomposites were then interacted with HEp-2 cells for *in vitro* imaging using dark-field scattering microscopy. In most cases, $Cu_{2-x}Se$/rGO nanocomposites bind on the cell membrane and present strong blue dark-field scattering light (Fig. 7D), while the cells treated with GO or $Cu_{2-x}Se$ NPs emit yellow-green light from cells or faint blue light (Fig. 7B and C). So, $Cu_{2-x}Se$/rGO nanocomposites with excellent affinity and biocompatibility could potentially be used for cell imaging *in vivo*.

What's more, anchoring $Cu_{2-x}Se$ NPs on rGO sheets, $Cu_{2-x}Se$/rGO nanocomposites exhibit an enhanced photothermal effect induced by NIR irradiation. Interestingly, the temperature of $Cu_{2-x}Se$/rGO aqueous solution (100 ug/mL) can be increased by 19.9 ℃ within 240 s NIR irradiation, compared with the temperature of pure water, GO and $Cu_{2-x}Se$ solution is only increased by 1.2 ℃, 3.4 ℃ and 12.1 ℃, respectively (Fig. S17). These data suggest that $Cu_{2-x}Se$/rGO nanocomposites can rapidly and efficiently convert the NIR laser energy into thermal energy, and further be potentially used for drug delivery and cancer therapy.

Conclusions

In this work, we have demonstrated a facile and green aqueous chemical method for the synthesis of highly self-doped $Cu_{2-x}Se$/rGO nanocomposites with a well-defined NIR LSPR at room-temperature, for the first time. GO was simultaneously reduced to rGO during the *in-situ* growth of $Cu_{2-x}Se$ NPs on the rGO sheets with the assistance of AA. This method might provide a convenient pathway to the preparation of cubic copper selenide/carbon nanomaterials structures. A proposed growth mechanism was discussed for the formation of $Cu_{2-x}Se$/rGO nanocomposites by verifying the intermediate product at different intervals of time in the synthesis. XRD and XPS analyses confirm the existence of cubic-phase $Cu_{2-x}Se$ on the rGO sheets containing Cu^{2+}, which comes from the solid-state conversion from $Cu_{2-x}Se$ ($x \approx 0$) to $Cu_{2-x}Se$ ($x > 0$) under oxidative conditions. As a result of cation vacancies within the crystal, the free carriers (holes) in the valence band of $Cu_{2-x}Se$ NPs increase as the oxidation proceeds, and a high concentration of free carriers leads to a strong NIR LSPR in $Cu_{2-x}Se$/rGO nanocomposites. With varying the reaction time, this NIR absorption band can be well-tuned as the free carriers (holes) changed, while the morphology and crystal phase of $Cu_{2-x}Se$ NPs on the rGO sheets remained. Thanks to the excellent biocompatibility of graphene, $Cu_{2-x}Se$/rGO nanocomposites exhibit good biocompatibility as well as unique optical properties, and are used for *in vitro* dark-field light scattering imaging of cancer cells. Furthermore, $Cu_{2-x}Se$/rGO nanocomposites with intense LSPR band at 1050 nm will possess huge potential in feature photothermal therapy.

Acknowledgements

This work was financially supported by the National Natural Science Foundation of China (NSFC, No 21375109) and the Cultivation Program of Chongqing Science & Technology Commission for 100 Outstanding Science and Technology Leading Talents.

Notes and references

[a] Key Laboratory of Luminescent and Real-Time Analytical Chemistry (Southwest University), Ministry of Education, College of Chemistry and Chemical Engineering, Southwest University, Chongqing 400715, China
[b] College of Pharmaceutical Science, Southwest University, Chongqing 400715, China

† Electronic Supplementary Information (ESI) available: [Experimental details，Particle size distribution histogram diagram of $Cu_{2-x}Se$ NPs on rGO sheets， AFM image， EDS spectrum， TGA curve, DTG curves, DLS spectra, ζ-potential spectra and dark field light scattering images of $Cu_{2-x}Se$/rGO nanocomposites]. See DOI: 10.1039/b000000x/

1. S. C. Riha, D. C. Johnson and A. L. Prieto, *J Am Chem Soc*, 2010, **133**, 1383-1390.
2. J. B. Zhu, Q. Y. Li, L. F. Bai, Y. F. Sun, M. Zhou and Y. Xie, *Chem. Eur. J.*, 2012, **18**, 13213-13221.
3. J. Choi, N. Kang, H. Y. Yang, H. J. Kim and S. U. Son, *Chem Mater*, 2010, **22**, 3586-3588.
4. S. Deka, A. Genovese, Y. Zhang, K. Miszta, G. Bertoni, R. Krahne, C. Giannini and L. Manna, *J Am Chem Soc*, 2010, **132**, 8912-8914.

5. X. Liu, X. Wang, B. Zhou, W.-C. Law, A. N. Cartwright and M. T. Swihart, *Adv Funct Mater*, 2013, **23**, 1256-1264.
6. J.-L. Yue, Q. Sun and Z.-W. Fu, *Chem Commun*, 2013, **49**, 5868-5870.
7. S. Liu, Z. Zhang, J. Bao, Y. Lan, W. Tu, M. Han and Z. Dai, *J. Phys. Chem. C*, 2013, **117**, 15164-15173.
8. S. Q. Lie, D. M. Wang, M. X. Gao and C. Z. Huang, *Nanoscale*, 2014, **6**, 10289-10296.
9. J. Xu, W. Zhang, Z. Yang, S. Ding, C. Zeng, L. Chen, Q. Wang and S. Yang, *Adv Funct Mater*, 2009, **19**, 1759-1766.
10. G. Xiao, Y. Zeng, Y. Jiang, J. Ning, W. Zheng, B. Liu, X. Chen, G. Zou and B. Zou, *Small*, 2013, **9**, 793-799.
11. Y. Zhao, H. Pan, Y. Lou, X. Qiu, J. Zhu and C. Burda, *J Am Chem Soc*, 2009, **131**, 4253-4261.
12. J. M. Luther, P. K. Jain, T. Ewers and A. P. Alivisatos, *Nat. Mater.*, 2011, **10**, 361-366.
13. D. Dorfs, T. Härtling, K. Miszta, N. C. Bigall, M. R. Kim, A. Genovese, A. Falqui, M. Povia and L. Manna, *J Am Chem Soc*, 2011, **133**, 11175-11180.
14. I. Kriegel, C. Jiang, J. Rodríguez-Fernández, R. D. Schaller, D. V. Talapin, E. da Como and J. Feldmann, *J Am Chem Soc*, 2011, **134**, 1583-1590.
15. S.-W. Hsu, K. On and A. R. Tao, *J Am Chem Soc*, 2011, **133**, 19072-19075.
16. I. Kriegel, J. Rodríguez-Fernández, A. Wisnet, H. Zhang, C. Waurisch, A. Eychmüller, A. Dubavik, A. O. Govorov and J. Feldmann, *ACS Nano*, 2013, **7**, 4367-4377.
17. W. Li, R. Zamani, P. Rivera Gil, B. Pelaz, M. Ibáñez, D. Cadavid, A. Shavel, R. A. Alvarez-Puebla, W. J. Parak, J. Arbiol and A. Cabot, *J Am Chem Soc*, 2013, **135**, 7098-7101.
18. Y. Zhao and C. Burda, *Energy Environ. Sci.*, 2012, **5**, 5564-5576.
19. X. Liu and M. T. Swihart, *Chem Soc Rev*, 2014, **43**, 3908-3920.
20. A. Comin and L. Manna, *Chem Soc Rev*, 2014, **43**, 3957-3975.
21. G. Ku, M. Zhou, S. Song, Q. Huang, J. Hazle and C. Li, *ACS Nano*, 2012, **6**, 7489-7496.
22. X. Liu, W.-C. Law, M. Jeon, X. Wang, M. Liu, C. Kim, P. N. Prasad and M. T. Swihart, *Adv. Healthcare Mater.*, 2013, **2**, 952-957.
23. C. M. Hessel, V. P. Pattani, M. Rasch, M. G. Panthani, B. Koo, J. W. Tunnell and B. A. Korgel, *Nano Lett.*, 2011, **11**, 2560-2566.
24. Q. Tian, F. Jiang, R. Zou, Q. Liu, Z. Chen, M. Zhu, S. Yang, J. Wang, J. Wang and J. Hu, *ACS Nano*, 2011, **5**, 9761-9771.
25. K. Dong, Z. Liu, Z. Li, J. Ren and X. Qu, *Adv Mater*, 2013, **25**, 4452-4458.
26. P. K. Jain, X. Huang, I. H. El-Sayed and M. A. El-Sayed, *Acc Chem Res*, 2008, **41**, 1578-1586.
27. Y. Xie, L. Carbone, C. Nobile, V. Grillo, S. D'Agostino, F. Della Sala, C. Giannini, D. Altamura, C. Oelsner, C. Kryschi and P. D. Cozzoli, *ACS Nano*, 2013, **7**, 7352-7369.
28. Q. Tian, J. Hu, Y. Zhu, R. Zou, Z. Chen, S. Yang, R. Li, Q. Su, Y. Han and X. Liu, *J Am Chem Soc*, 2013, **135**, 8571-8577.
29. X. Liu, C. Lee, W.-C. Law, D. Zhu, M. Liu, M. Jeon, J. Kim, P. N. Prasad, C. Kim and M. T. Swihart, *Nano Lett.*, 2013, **13**, 4333-4339.
30. J. G. Radich, R. Dwyer and P. V. Kamat, *J. Phys. Chem. Lett.*, 2011, **2**, 2453-2460.
31. Y. Su, X. Lu, M. Xie, H. Geng, H. Wei, Z. Yang and Y. Zhang, *Nanoscale*, 2013, **5**, 8889-8893.
32. J. Bai and X. Jiang, *Anal Chem*, 2013, **85**, 8095-8101.
33. G. Nie, L. Zhang, X. Lu, X. Bian, W. Sun and C. Wang, *Dalton Trans*, 2013, **42**, 14006-14013.
34. Y. Zhang, J. Tian, H. Li, L. Wang, X. Qin, A. M. Asiri, A. O. Al-Youbi and X. Sun, *Langmuir*, 2012, **28**, 12893-12900.
35. L. F. Zhang and C. Y. Zhang, *Nanoscale*, 2014, **6**, 1782-1789.
36. W. L. Fu, S. J. Zhen and C. Z. Huang, *Analyst*, 2013, **138**, 3075-3081.
37. K. Liu, J.-J. Zhang, F.-F. Cheng, T.-T. Zheng, C. Wang and J.-J. Zhu, *J Mater Chem*, 2011, **21**, 12034-12040.
38. Y. Tao, Y. Lin, Z. Huang, J. Ren and X. Qu, *Adv Mater*, 2013, **25**, 2594-2599.
39. M. Yin, L. Wu, Z. Li, J. Ren and X. Qu, *Nanoscale*, 2012, **4**, 400-404.
40. C. Xu, X. Wang and J. Zhu, *J Phys Chem C*, 2008, **112**, 19841-19845.
41. B. Li, H. Cao, G. Yin, Y. Lu and J. Yin, *J Mater Chem*, 2011, **21**, 10645-10648.
42. J. Zhang, H. Yang, G. Shen, P. Cheng, J. Zhang and S. Guo, *Chem Commun*, 2010, **46**, 1112-1114.
43. M. J. Fernández-Merino, L. Guardia, J. I. Paredes, S. Villar-Rodil, P. Solís-Fernández, A. Martínez-Alonso and J. M. D. Tascón, *J. Phys. Chem. C*, 2010, **114**, 6426-6432.
44. X. M. Zhao, S. W. Zhou, L. P. Jiang, W. H. Hou, Q. M. Shen and J. J. Zhu, *Chem. Eur. J.*, 2012, **18**, 4974-4981.
45. Z. Ren, Y. Wei, J. Xiang, S. Zhang, J. Song, C. Mao, H. Niu, B. Jin, J. Wu and Y. Tian, *Anal Lett*, 2013, **46**, 1394-1403.
46. F. X. Rong, Y. Bai, T. F. Chen and W. J. Zheng, *Mater Res Bull*, 2012, **47**, 92-95.
47. Y. Liu and C. Z. Huang, *Nanoscale*, 2013, **5**, 7458-7466.
48. Y. Liu and C. Z. Huang, *ACS Nano*, 2013, **7**, 11026-11034.
49. R. Hu, K.-T. Yong, I. Roy, H. Ding, S. He and P. N. Prasad, *J. Phys. Chem. C*, 2009, **113**, 2676-2684.
50. L. Zhang, S. J. Zhen, Y. Sang, J. Y. Li, Y. Wang, L. Zhan, L. Peng, J. Wang, Y. F. Li and C. Z. Huang, *Chem Commun*, 2010, **46**, 4303-4305.
51. Y. Wang, S. J. Zhen, Y. Zhang, Y. F. Li and C. Z. Huang, *J. Phys. Chem. C*, 2011, **115**, 12815-12821.
52. X.-Y. Wan, L.-L. Zheng, P.-F. Gao, X.-X. Yang, C.-M. Li, Y. F. Li and C. Z. Huang, *Sci. Rep.*, 2014, **4**, 4529.